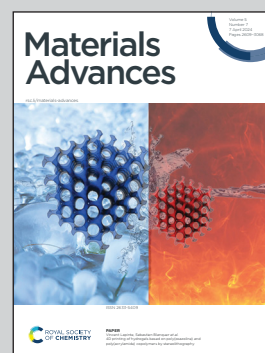**Showcasing research from Professor Ujjwal Pal's laboratory, Department of Energy and Environmental Engineering, CSIR-Indian Institute of Chemical Technology, Hyderabad, INDIA.**

Defect-rich UiO-66@g-C$_3$N$_4$/Ni frameworks as efficient water splitting photocatalyst

We have showcased the creation of defect-rich UiO-66@g-C$_3$N$_4$/Ni frameworks featuring heterojunction, greatly improved charge generation and separation, and thus significantly enhanced the photocatalytic activity and stability compared with the non-defect UiO-66 based hybrid photocatalyst.

As featured in:

See Ujjwal Pal *et al.*,
Mater. Adv., 2024, **5**, 2785.

ROYAL SOCIETY
OF **CHEMISTRY**

rsc.li/materials-advances

PAPER

Check for updates

Defect-rich UiO-66@g-C$_3$N$_4$/Ni frameworks as efficient water splitting photocatalysts†

Aparna Jamma,[ab] Bhavya Jaksani,[ab] Chandra Shobha Vennapoosa,[ab] Spandana Gonuguntla,[ab] Saddam Sk, [iD][ab] Mohsen Ahmadipour,[c] Moses Abraham B., [iD][d] Indranil Mondal [iD][e] and Ujjwal Pal [iD]*[ab]

In this report, we uncover the synergistic role of g-C$_3$N$_4$, a cocatalyst (Ni), and defect sites of Zr-MOFs for unprecedented hydrogen evolution activity. Further, the interaction between defect rich UiO-66-D and g-C$_3$N$_4$ is well-supported by theoretical understanding and photocatalysis trends. The key role in the enhanced activity is further substantiated by considering the abundant type-II heterojunction between UiO-66-D and g-C$_3$N$_4$ in the hybrid composite. This study emphasizes the significance of defect-induced local strain and modification of the electronic structure at the junction connecting UiO-66 and g-C$_3$N$_4$ along with Ni NPs, demonstrating their role in the catalytic activity. Ligand oriented defect engineering is deliberately utilized to manipulate photonic and electrical attributes of the UiO-66 framework. Improved catalytic performance is ascribed to structural stabilization of the composite by the introduction of unsaturation in UiO-66 and suitable coordinated Ni NPs over g-C$_3$N$_4$, resulting in a multi-fold enhancement of the hydrogen production rate of 2.6 mmol g^{-1} h^{-1} with an AQY of 6.41% at 420 nm as compared to the pristine material.

Introduction

The widespread utilization of fossil fuels in contemporary industries has attracted attention to and resulted in concern regarding environmental issues and energy-related challenges. In response, solar energy has emerged as a highly promising alternative due to its clean, renewable, and abundant nature, demonstrating its potential as a viable solution to mitigate exhaust emissions. The application of renewable energy for light-driven hydrogen generation through water represents a viable and eco-friendly alternative. However, the key obstacle lies in the development of photocatalysts that exhibit exceptional efficiency and durability. In a broader context, an exemplary photocatalyst should possess the following attributes: notable light absorption in the visible spectrum, prolonged excited state

lifetime, superior efficiency in charge separation, and enhanced charge mobility.[1–4]

Metal–organic frameworks (MOFs) have become evident as extraordinary materials for hydrogen generation as a consequence of their good porosity, internal surface areas, diverse topologies, and chemical stability. A set of metal–organic frameworks (MOFs) based on Zr exhibiting UiO-type structures have been successfully synthesized, and could be used in visible-light-driven photocatalytic hydrogen generation, capitalizing on the linker-to-metal charge transfer (LMCT) phenomenon. These MOFs display exceptional photocatalytic activity owing to their exceptional thermal and chemical stability. The coordination interaction between Zr ions and carboxylate ligands exhibits remarkable strength, enabling the as-prepared metal–organic frameworks (MOFs) to withstand the rigorous conditions of base catalysis during hydrogen (H$_2$) generation. Nevertheless, the insufficient photoreactivity of perfect MOFs imposes limitations on their functional implementations, so further work is needed in the realm of structural engineering of MOFs. This work is essential for charge migration over the surface, and optimizing the utilization of catalytic centers, thus maximizing the exposure to achieve superior performance.[5–7]

The enhancement of bulk charge transfer can be achieved through defect tailoring, enabling the enhancement of charge carrier transport. This involves the deliberate introduction of defects by breaking linkages within the organic linkers. The regulation of defects within semiconductors can change the

[a] Department of Energy & Environmental Engineering, CSIR Indian Institute of Chemical Technology, Tarnaka, Hyderabad, Telangana, 500007, India. E-mail: upal03@gmail.com, ujjwalpal@iict.res.in

[b] Academy of Scientific and Innovative Research (AcSIR), Ghaziabad – 201002, India

[c] Institute of Power Engineering, Universiti Tenaga Nasional, Kajang, 43000, Selangor, Malaysia

[d] Department of Chemical Engineering, Indian Institute of Technology Kanpur, Kanpur, 208016, India

[e] School of Chemistry, Indian Institute of Science Education and Research Thiruvananthapuram, Vithura, Thiruvananthapuram 695551, India

† Electronic supplementary information (ESI) available. See DOI: https://doi.org/10.1039/d3ma00880k

electronic structure of materials and modulate the excited state charge carriers. Additionally, when viewed from the standpoint of surface chemistry, the coordinatively unsaturated sites linked to surface defects play the role of active sites and expedite the rapid absorption and activation of reactant molecules.[8] Previous theoretical investigations have suggested that eliminating linkers within UiO-66 results in a reduction of energy levels within the unoccupied d orbitals of zirconium (Zr) atoms. This change potentially increases the probability of facilitating charge transfer during the photocatalytic process.[9,10] Additionally, it has been observed in the recent studies of our group that defects control the recombination in the HER.[11] The linkers are believed to function as recombination sites for minority charge carriers. Consequently, the process disrupts the regular grouping of atoms/ions in the primary structure. Expanding on this concept, Zhao et al. achieved the successful fabrication of defective heterojunction NU66-d/ZIS photocatalysts through a silver-catalyzed decarboxylation method, showcasing remarkable photocatalytic activity.[12] Jiang et al. conducted a study on UiO-66-NH$_2$ with varying degrees of structural defects to investigate its performance in photocatalytic hydrogen (H$_2$) production. Pt nanoparticles were incorporated as co-catalysts in the system.[13] In our prior research, we investigated the photoactivity of a titanium MOF.[2] Additionally, we explored a noble metal-free system consisting of PANI-sensitized Co$_3$O$_4$ modified with both defect-free and defective metal–organic frameworks (MOFs) (M = Ti, Zr).[14,15]

Recently, graphitic carbon nitride (g-C$_3$N$_4$) has attracted considerable attention in various photocatalytic applications as a metal-free polymeric semiconductor. This attention stems from its exceptional electrical, optical, conductive, photonic, and material characteristics, accentuated by its ductile layered construction, reminiscent of graphite oxide. This character enables g-C$_3$N$_4$ to establish anchoring and wrapping interactions with host materials or substrates such as UiO-66, thereby establishing proximity interfaces connecting UiO-66 and g-C$_3$N$_4$ materials.[16] In general, composites incorporating graphitic carbon nitride (g-C$_3$N$_4$) showcase improved photocatalytic performance attributed to increased chemical heterogeneity and efficient interfacial charge transfer from photoexcited g-C$_3$N$_4$ to the host materials. Wang et al. successfully synthesized Zr-containing metal–organic framework (MOF) UiO-66/g-C$_3$N$_4$ hybrids through thermal annealing. These hybrids exhibited improved photocatalytic hydrogen (H$_2$) production under visible-light illumination.[17] Moreover, the integration of g-C$_3$N$_4$ with diverse materials, such as MIL-125(Ti),[18] Cu-BTC,[19] NH$_2$-MIL-88B(Fe), UiO-66, and ZIF-8,[20] has shown notable improvements in electron–hole separation capabilities and a notable enhancement in the photocatalytic activity of the resultant catalysts.

Researchers are actively seeking economical, highly effective, and durable noble-metal-free materials to serve as cocatalysts for photocatalytic hydrogen (H$_2$) production when exploring noble metals. An alternative methodology entails incorporating a compatible co-catalyst with resilient light-absorbing substances, acting as a supplementary tactic to enhance the conversion efficiency of solar energy for hydrogen (H$_2$) generation, owing to the interface impact.[21] In this context, a plethora of materials derived from

abundant elements such as iron (Fe), cobalt (Co), nickel (Ni), and molybdenum (Mo) have been extensively investigated and utilized as cocatalysts. Within these cocatalysts, the incorporation of nickel nanoparticles (Ni NPs) serves as an efficient means to harness light, resulting in increased visible-light absorption and the subsequent generation of a greater number of electron–hole pairs. Nickel, known for its abundance, serves as a typical promoter for hydrogen evolution, exhibiting outstanding photostability and a strong ability to enhance the photocatalytic process for HER. The incorporation of Ni-deposition enhances the electronic structure of the MOF composite, boosting its ability to separate charges, thereby reducing the recombination of photogenerated holes and electrons.[22–24] Furthermore, Ni NPs facilitate efficient energy transfer to the conduction band (CB) of the semiconductor. Notably, Ni nanoparticles exhibit remarkable catalytic activity and have garnered attention as co-catalysts for hydrogen (H$_2$) evolution generation.

In this study, our objective was to enhance the relative photocatalytic efficiencies of composite materials comprising pristine along with defective UiO-66 integrated with g-C$_3$N$_4$ and Ni nanoparticles (NPs) as co-catalysts. Initially, unaltered UiO-66 was fabricated employing the traditional solvothermal approach. Subsequently, defect engineering was employed to further tailor the functionalities of UiO-66, utilizing the silver-catalyzed decarboxylation method (Fig. 1(a)). The detailed synthesis and experimental work are discussed in the ESI† (S1). Ni NPs acted as a cocatalyst in this photocatalytic hydrogen evolution system, and stabilization was through C and N of g-C$_3$N$_4$ and –OH/OH$_2$ species of the UiO-66 MOF.[25,26] The structural configuration and mechanistic approach responsible for the enhanced efficiency of H$_2$ evolution of the eosin Y (EY) sensitized UiO-66-D@g-C$_3$N$_4$/Ni heterostructure were systematically investigated. The junction formed at the interface of UiO-66-D and g-C$_3$N$_4$ creates an unobstructed route for efficient photoinduced charge transfer, promoting the efficient dissociation of photogenerated electron–hole pairs.

Results and discussion

The solvothermal heating of ZrCl$_4$ and terephthalic acid in DMF led to a highly crystalline MOF with octahedral type morphology. The crystallinity did not disrupt and no new species formed after partial decarboxylation of the MOF (UiO-66 JCPDS: 4512072). The degree of crystallinity in UiO-66 and its composites was assessed using powder X-ray diffraction (XRD), as depicted in Fig. 1(b). The diffraction peaks at 2θ values of 7.54, 8.7, 25.9, and 28.2 represent the (111), (002), (224), and (046) phase structures of the UiO-66 MOF. These findings imply the crystallinity of the final structures. A loading amount of 10–50 wt% of g-C$_3$N$_4$ co-exists well with the defective MOF and does not have any impact on the MOF crystallinity (Fig. 1(b) and Fig. S3(a), (b), ESI†). The solvothermal reduction of nickel salt in the presence of the g-C$_3$N$_4$/MOF composite successfully resulted in a Ni/g-C$_3$N$_4$/MOF heterostructure ([220] exposed facet and cubic crystal structure) being dispersed,
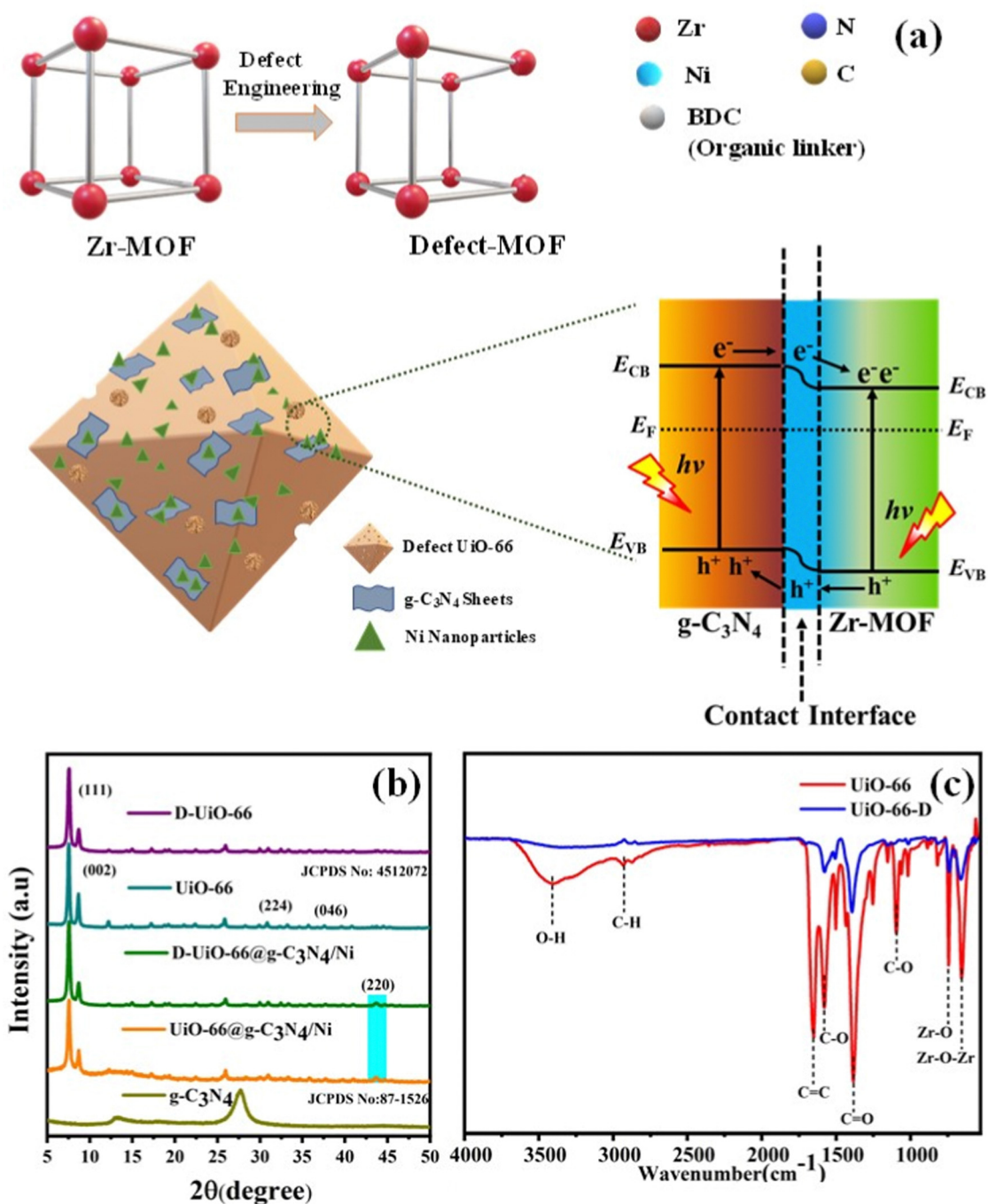
Fig. 1 (a) Synergistic role of g-C_3N_4, the heterojunction between UiO-66@g-C_3N_4 and Ni NPs in the g-C_3N_4/UiO-66-D/Ni hybrid composite; (b) XRD analysis of the *in situ* fabricated photocatalysts; and (c) FTIR analysis of pristine and defective UiO-66 photocatalysts.

located homogeneously throughout the composite. The X-ray diffraction (XRD) pattern of nickel (Ni) exhibited a distinct diffraction peak at 44.5 degrees, corresponding to the indexing of (220) crystal planes. This observation confirms the presence of a cubic crystal structure, in excellent agreement with the reported literature value (JCPDS 78-0423).[27] The linker-oriented defects (decarboxylation) were confirmed by a substantial loss of C=O stretching intensity in the FTIR analysis as shown in Fig. 1(c). The vibration stretching at 1583, 1437, and 1388 cm^{-1}

is due to the asymmetric stretching of the carboxyl groups. The vibrational stretching at 747 cm^{-1} and 660 cm^{-1} was assigned to the M–O bonding (M = Zr) (as shown in Fig. S2, ESI† and Fig. 1(c)).

The morphology of the UiO-66 was not retained after decarboxylation and turned into porous unordered crystallites as confirmed by the SEM and TEM analysis (Fig. 2(a)–(e) and Fig. S4, ESI†). We expect this kind of morphology with a rough surface that tends to facilitate a strong anchoring of g-C_3N_4 and
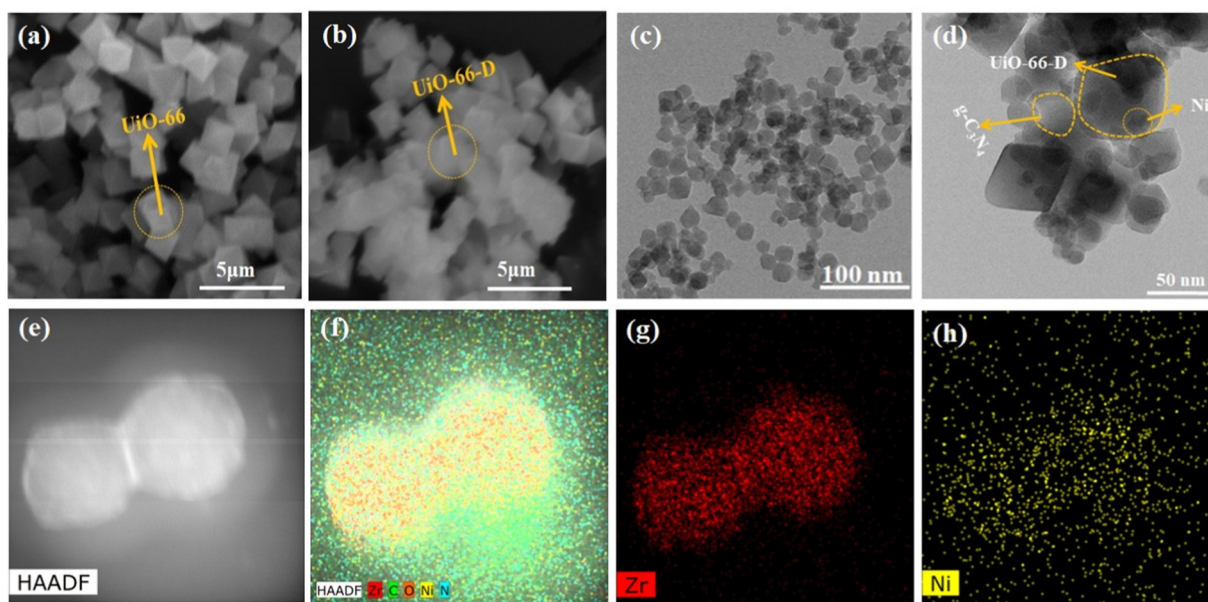
Fig. 2 SEM images of (a) UiO-66 and (b) UiO-66-D; TEM analysis of (c) UiO-66 and (d) UiO-66-D@g-C$_3$N$_4$/Ni; (e) and (f) HADAF analysis; elemental analysis of (g) Zr and (h) Ni. (Due to the low content of Ni in the MOF composite, we observe the HAADF image with a low signal).

Ni nanoparticles, thus helping to obtain small-size heterojunctions. The co-existence of g-C$_3$N$_4$ and Ni on the MOF surface has been successfully confirmed by the detection of exposed planes of the respective components in HRTEM. The loading of nickel nanoparticles onto UiO-66@g-C$_3$N$_4$ is illustrated in Fig. S4(c) (ESI†). In Fig. S4(b) (ESI†), in the HR-TEM image, the observed fringes have spacings of approximately 0.17 nm and 0.21 nm, which can be attributed to (220) and (111) lattice planes, respectively, of nickel (Ni). Fig. 2(d) depicts the HR-TEM image of UiO-66-D@g-C$_3$N$_4$/Ni. EDAX analysis confirmed the presence of approximately 1–2% of Ni for all the composites, and morphological variations of g-C$_3$N$_4$, UiO-66@g-C$_3$N$_4$, and UiO-66-D@g-C$_3$N$_4$ were observed, as depicted in Fig. S6 (ESI†). The high-angle annular dark-field image along with corresponding elemental mapping confirms that there is no phase separation of the MOF components. Moreover, the MOF crystals are only externally covered with g-C$_3$N$_4$ and metallic Ni. The occurrence of various elements including Ni, Zr, N, C, and O was observed, as shown in Fig. 2(e)–(h) and Fig. S5 (ESI†).

The optical properties of the MOF were altered due to decarboxylation. The white colour of the UiO-66 (with a band gap of 3.9 eV) changed to a pale brown colour with an estimated band gap of 3.5 eV (Fig. 3(a) and (b)). This alteration in light-harvesting capability can be attributed to structural defects or variations in particle size.[28–30] These modifications render UiO-66-D a more effective material for capturing visible light, potentially enhancing its photocatalytic activity. The bandgap of g-C$_3$N$_4$ was calculated as 2.6 eV (Fig. S7, ESI†), which apparently could improve the light harvesting ability of the overall composite. From the band gap estimation, it can be assumed that the MOF and g-C$_3$N$_4$ are likely to form a type-II heterojunction, which can direct the charge carrier transfer

during photoirradiation. This has been well reflected in the time dependent photoluminescence (PL) analysis. We monitored the photoluminescence (PL) response originating from the MOF to track the charge carrier transfer/recombination caused by it. The PL spectra of the pristine, defect rich MOF and the individual composites were recorded with excitation at 350 nm. As illustrated in Fig. 3(c), UiO-66 shows the highest PL emission intensity, which was attributed to the surface charge recombination properties of the UiO-66 material.[31] The observed decrease in photoluminescence (PL) intensity for UiO-66-D is associated with structural defects within the UiO-66. These defects create additional pathways for the migration of photo-generated electrons. As a result, photo-generated electron–holes exhibit longer lifetimes, contributing to the decrease in PL intensity.[32] When UiO-66 was combined with g-C$_3$N$_4$, there was a nearly complete quenching of the photoluminescence (PL), indicating a rapid charge transfer process that effectively suppressed the radiative decay within MOF energy states. This outcome highlights the synergistic effect between UiO-66 and g-C$_3$N$_4$, which increases the possibility of efficient electron–hole separation. Consequently, the photocatalytic activities of the composite material surpassed those of the individual pure materials.[33,34]

Subsequently, to examine the recombination kinetics of the charge carriers, time-resolved photoluminescence decay spectra were recorded, employing the time-correlated single-photon counting (TCSPC) method. As shown in Fig. 3(d), the spectra of UiO-66, UiO-66@g-C$_3$N$_4$/Ni, and UiO-66-D@g-C$_3$N$_4$/Ni were fitted well with a tri-exponential decay process, and the decay profile of UiO-66-D could be fitted as a bi-exponential decay, where the measured lifetime decay values were 3.70 ns for UiO-66-D@g-C$_3$N$_4$/Ni, 3.08 ns for non-defective UiO-66-D@g-C$_3$N$_4$/Ni, 1.62 ns for pristine UiO-66 MOF, and 1.82 ns for defective
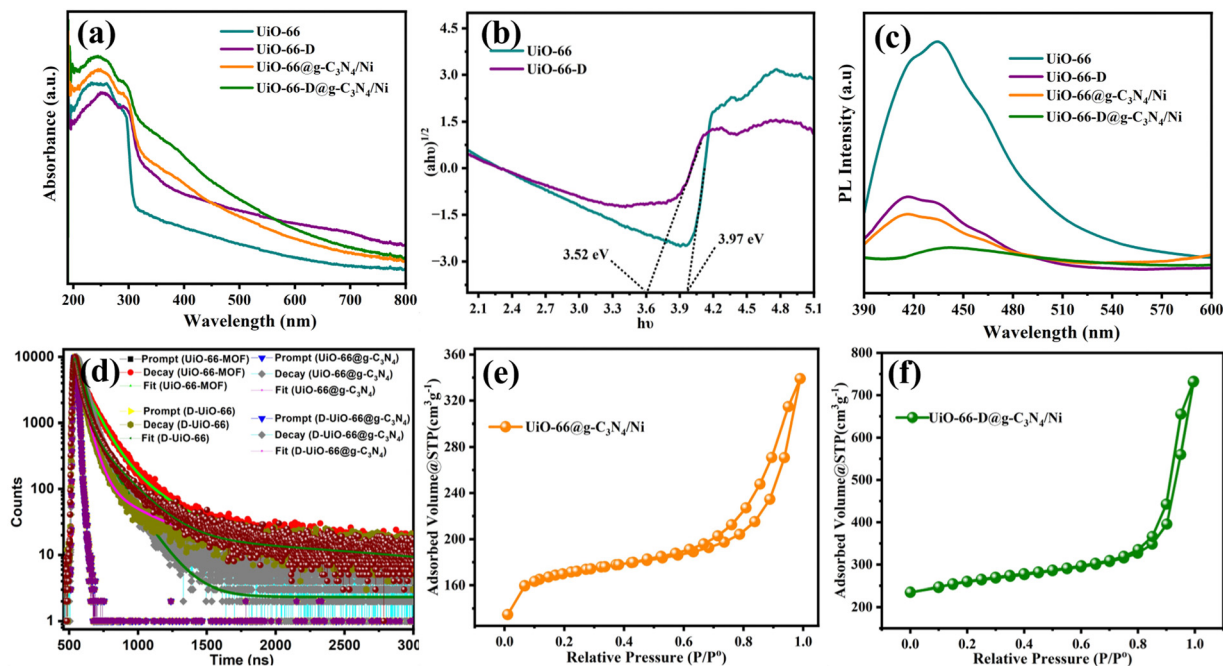
Fig. 3 (a) UV-vis DRS studies of the composites; (b) Tauc plots, (c) PL spectra, and (d) TCSPC of the prepared samples; N_2 adsorption–desorption isotherms of (e) UiO-66@g-C_3N_4/Ni and (f) UiO-66-D@g-C_3N_4/Ni.

UiO-66 MOF, as summarized in Table S3 (ESI†). The shorter PL lifetime in the UiO-66-D@g-C_3N_4/Ni hybrid confirms the fast transfer of photogenerated electrons from g-C_3N_4 to UiO-66, thereby suppressing the recombination of electron–hole pairs.

The porosity characteristics of the defective and non-defective photocatalysts were determined by analysing nitrogen adsorption–desorption isotherms using BET and BJH characterization techniques, as illustrated in Fig. 3(e) and (f) and Fig. S8 (ESI†). The calculated S_{BET} values for g-C_3N_4, UiO-66, UiO-66-D, UiO-66@g-C_3N_4/Ni, and UiO-66-D@g-C_3N_4/Ni were 394.2, 858.1, 907.9, 549.9, and 808.9 m^2 g^{-1}, respectively. The surface area of the defective MOFs is relatively high. Similarly, we note that the UiO-66-D@Ni/g-C_3N_4 UiO-66-D@g-C_3N_4/Ni exhibits a higher surface area compared to UiO-66@Ni/g-C_3N_4 UiO-66@g-C_3N_4/Ni. On the other hand, UiO-66@Ni/g-C_3N_4 UiO-66@g-C_3N_4/Ni showed a reduced surface area on the addition of g-C_3N_4 due to reduced crystallinity, whereas due to increased defects and alterations in crystallinity, the UiO-66-D@Ni/g-C_3N_4 UiO-66-D@g-C_3N_4/Ni showed a significantly high value.[35] The isotherms exhibited type IV hysteresis, which indicates the presence of mesopores (sizes between 2 and 50 nm). The data regarding the specific surface area, pore volume, and mean pore diameter can be found in Table S2 (ESI†). Linker vacancies in the UiO-66 framework result in open sites, leading to an expanded accessible surface area. This generally correlates positively, indicating that higher linker vacancies tend to correspond with a greater BET surface area in UiO-66.[36]

The thermal stabilities of UiO-66 and its composites were determined using the TGA curves in Fig. S9(a) and (b) (ESI†). The TGA curve of UiO-66 indicates that it has thermal stability up to 600 °C. The TGA result confirms the high thermal stability of UiO-66, resulting in its morphology and composition under sunlight conditions.[37]

EPR spectroscopy is a useful method used to investigate the paramagnetic attributes of both pristine and defective UiO-66, which pertain to the presence of unpaired electrons within the material. As illustrated in Fig. 5(c), the presence of low-intensity signals was observed in the defect-containing composite material (UiO-66-D@g-C_3N_4/Ni). Remarkably, a unique electron paramagnetic resonance (EPR) signal at a g-value of 2.07 was apparent in the MOF without defects (UiO-66). This signal is indicative of the presence of Zr^{3+}, definitively confirming the presence of defects in UiO-66.

To comprehensively examine the elemental surface composition and oxidation states, X-ray photoelectron spectroscopy (XPS) analysis was performed on both the pristine UiO-66@g-C_3N_4/Ni and defective UiO-66-D@g-C_3N_4 UiO-66-D@g-C_3N_4/Ni photocatalysts. The full scan XPS reveals the existence of Zr, Ni, C, N, and O, which can be correlated to their respective binding energy positions, as depicted in Fig. 4(a). These findings demonstrate strong concurrence with the results obtained from inductively coupled plasma (ICP) analysis.

In the high-resolution X-ray photoelectron spectra (XPS) of the Ni 2p region, distinct peaks were observed at binding energies around 856.2 eV and 879.6 eV, representing the Ni $2p_{3/2}$ and Ni $2p_{1/2}$ spin–orbit components, respectively. Additionally, two satellite peaks were identified at 861.9 eV and 880.2 eV (Fig. 4(b)). These peaks confirmed that the valence of the installed Ni ions is +2, with Ni–C bonding.[38] The above findings indicate that when exposed to air, a portion of Ni NPs undergo oxidation. The Zr 3d spectrum (Fig. 4(c)) exhibited
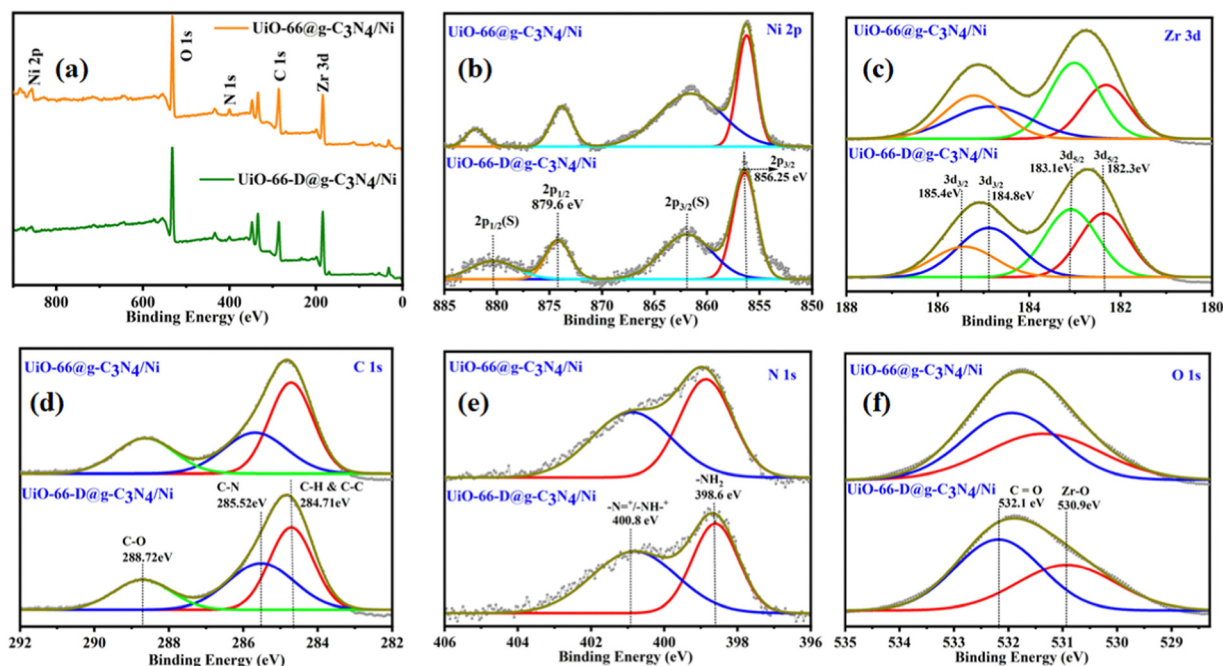
Fig. 4 XPS spectra of UiO-66@g-C$_3$N$_4$/Ni and UiO-66-D@g-C$_3$N$_4$/Ni composites: (a) survey spectra, (b) Ni 2p, (c) Zr 3d, (d) C 1s, (e) N 1s, and (f) O 1s.
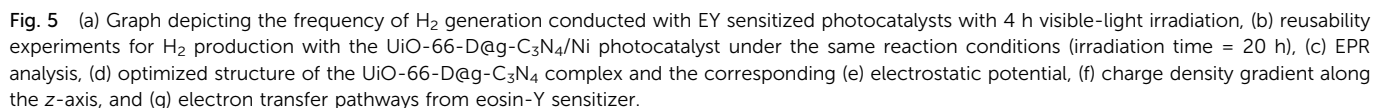
peaks at binding energies of approximately 182.3 and 183.1 eV, corresponding to Zr 3d$^{5/2}$, and 184.8 and 185.4 eV, corresponding to Zr 3d$^{3/2}$ spin–orbit components. These peaks unequivocally substantiated the existence of Zr^{4+}. In the C 1s region, peaks were observed at binding energies of approximately 284.71 eV (Fig. 4(d)), corresponding to the sp^2 hybridized carbon atoms in g-C$_3$N$_4$ and graphitic carbon. Other peaks were detected at around 288.72 eV for C–O, and 285.52 eV, signifying the existence of C–N species within the g-C$_3$N$_4$ structure. The N 1s region displayed peaks centred at binding energies of approximately 400.8 eV, corresponding to the pyridinic and graphitic nitrogen species in g-C$_3$N$_4$. Additionally, a peak at 398.6 eV indicated the presence of amino (–NH$_2$) groups in the g-C$_3$N$_4$ structure (Fig. 4(e)). The O 1s spectrum revealed peaks at approximately 532.1 and 530.9 eV, ascribed to C=O and Zr–O, respectively, which can be assigned to the lattice oxygen in the defect engineered UiO-66 (Fig. 4(f)). The XPS results confirm that the chemical states of UiO-66 and g-C$_3$N$_4$ remain unaltered following the synthesis process.

Photocatalytic hydrogen generation

The efficiency of hydrogen generation when exposed to solar light was measured for all the materials that were synthesized. This measurement was conducted in 20 mL of aqueous 10% (v/v) TEOA and eosin Y (EY) photosensitizer mixture at neutral pH under simulated light irradiation of $\lambda \geq 420$ nm (additional information can be found in the Electronic (ESI†)). As depicted in Fig. 5(a), the photocatalytic hydrogen generation rate of UiO-66-D experiences an improved enhancement

of approximately 1.5 times when compared to the pristine UiO-66, suggesting that structural defect sites play a critical role in photocatalysis. Prior theoretical investigations have suggested that the removal of linkers within UiO-66 results in a reduction of the energy levels of the unoccupied d orbitals of the Zr atoms. This reduction in energy levels may, in turn, enhance the probability of charge transfer during the photocatalytic process.[39] The EY-sensitized UiO-66-D@g-C$_3$N$_4$ UiO-66-D@g-C$_3$N$_4$/Ni shows better results in comparison to those of the pristine UiO-66@g-C$_3$N$_4$ UiO-66@g-C$_3$N$_4$/Ni. We further optimized the loading percentages of the Ni co-catalyst compared to the photocatalytic activity with other catalysts (Fig. S11(b) and Table S4 (ESI†)). Interestingly, the H$_2$ production rate for UiO-66-D@g-C$_3$N$_4$/Ni (2.0%) achieved ∼2621 μmol h^{-1} g^{-1} with an apparent quantum yield (AQY) of 6.41%, which surpasses the performance of the UiO-66@g-C$_3$N$_4$/Ni (∼2057 μmol h^{-1} g^{-1}) photocatalyst. The appropriate combination of the g-C$_3$N$_4$, metal–ligand properties and redox active Zr^{3+} ion led to an increased H$_2$ production rate, which is 25.4 times higher than that for the previously reported Zr-MOF benchmark photocatalysts.[40] On the other hand, the hydrogen generation efficiency of the photocatalysts without the g-C$_3$N$_4$ is low. This outcome substantiates the concept that the creation of UiO-66-D@g-C$_3$N$_4$/Ni heterojunctions results in a modified surface, thereby facilitating the enhanced separation of photogenerated electrons and holes. This, in turn, leads to improved photocatalytic activities. Based on these findings, it is evident that the generation of H$_2$ during the production reaction was facilitated by the absorption of incident light by EY. To gain a deeper insight into the merits of our photocatalyst, we have compiled the latest research outcomes in Table S5 (ESI†) Recyclability tests showed that the activity of the UiO-66-D@g-C$_3$N$_4$/Ni (2.0%) was good after five cycles of photocatalysis

Fig. 5 (a) Graph depicting the frequency of H_2 generation conducted with EY sensitized photocatalysts with 4 h visible-light irradiation, (b) reusability experiments for H_2 production with the UiO-66-D@g-C_3N_4/Ni photocatalyst under the same reaction conditions (irradiation time = 20 h), (c) EPR analysis, (d) optimized structure of the UiO-66-D@g-C_3N_4 complex and the corresponding (e) electrostatic potential, (f) charge density gradient along the z-axis, and (g) electron transfer pathways from eosin-Y sensitizer.

reaction under the same reaction conditions (Fig. 5(b)). The catalytic activity remained largely unaffected during the initial three cycles, but showed a slight decline in subsequent cycles, potentially attributed to surface dissolution or alterations in the local structure. The efficiency of the most effective catalyst was assessed for photocatalytic performance by examining the wavelength-specific AQY (quantum yield) across different monochromatic light sources (λ = 420, 550, 600, 700, and 800 ± 10 nm) using specific narrow band-pass filters. Subsequently, the AQY values corresponding to these wavelengths were computed by correlating the amount of

H_2 produced and the intensity of the incident monochromatic light, as per eqn (1).

$$AQY = 2 \times \text{number of evolved } H_2 \text{ molecules/number}$$
$$\text{of incident photons} \times 100 \quad (1)$$

As depicted in Fig. S11 (ESI†), the trend in AQY values for UiO-66-D@g-C_3N_4/Ni is closely related to the corresponding DRS spectra. Notably, UiO-66-D@g-C_3N_4/Ni demonstrates note-worthy AQY values of 6.41, 4.46, 3.27, 1.7, and 0.05% when

exposed to incident light at wavelengths of approximately 420, 550, 600, 700, and 800 $\pm$ 10 nm, respectively.[41–43]

In Fig. S11(a) (ESI†), the influence of pH on the generation of H_2 is depicted. The rate of hydrogen production was investigated across various pH levels (3, 7, and 12), revealing that neutral pH exhibited superior results compared to both acidic and basic pH conditions. The reduction in the rate of H_2 formation at acidic pH is probably due to the protonation of TEOA, which consequently hinders its efficiency as an electron donor. On the other hand, at basic pH, the thermodynamic driving force for H_2 formation from water diminishes, and this is crucial in the proposed mechanism of H_2 formation, and becomes unfavourable. An electrically balanced solution with a pH of 7.0, where both protonated and unprotonated forms of $TEOA^+$ (triethanolamine cation) coexist, was selected for subsequent experiments based on the findings of laboratory tests. This particular solution demonstrated the highest rate of hydrogen generation, prompting its utilization in further investigations.[44]

Mechanism of the enhanced photocatalytic H_2 production

After the analysis discussed, we proposed a photocatalytic mechanism for redox reaction in EY-sensitized UiO-66-D@g-C_3N_4/Ni composites. g-C_3N_4 and Ni attached onto the binding sites of UiO-66-D, establishing a shared active surface displaying diverse degrees of unsaturation. These sites of coordinated unsaturation expanded along the edges of this system, thereby creating additional active sites. Under visible light irradiation, the system's surface-bound EY absorbs light photons, leading to the formation of a singlet excited state (EY1*), followed by subsequent transformation into EY3* through intersystem crossing (ISC). TEOA effectively quenches EY3*, leading to the formation of $EY^{\bullet-}$.[45] Subsequently, electrons are transferred either directly from $EY^{\bullet-}$ to the Zr clusters, the conduction band (CB) of g-C_3N_4, or the loaded Ni co-catalysts (Fig. 5(g)). Furthermore, g-C_3N_4 can also undergo excitation, leading to the generation of electrons. These photoexcited electrons on the surface of g-C_3N_4 are then injected into the loaded Ni, facilitating the reduction of protons and subsequently forming molecular H_2. Alternatively, upon photon absorption by the ligand H_2BDC, the photogenerated and injected electrons, originating either from the CB of g-C_3N_4 or $EY^{\bullet-}$, are transferred to the Zr^{4+} within the Zr cluster, leading to the generation of Zr^{3+}. The intimate interfacial connections between g-C_3N_4 and UiO-66-D facilitate the efficient electron transfer responsible for this phenomenon. Consequently, the photoinduced electrons and holes experience increased spatial separation, effectively impeding the recombination of electron–hole pairs and thereby enhancing photoactivity. Ultimately, the protons gathered on the surface of UiO-66-D@g-C_3N_4 are conveyed to the Ni co-catalysts, where they undergo a reaction with electrons to generate H_2. TEOA, serving as an electron donor, consumes the holes in the valence band of g-C_3N_4 and the organic linker.

The electron migration pathway is supported by the observed reduction in the photoluminescence (PL) intensity of UiO-66-D@g-C_3N_4/Ni.

Thus, the enhanced H_2 evolution performance can be ascribed to the following reasons, attributed to the presence of UiO-66-D: (1) UiO-66-D exhibits a substantial specific surface area supporting the formation of a heterostructure between UiO-66-D and g-C_3N_4, resulting in an intimate contact interface and facilitating the effective dispersion of Ni co-catalysts. (2) The porous MOFs act as efficient electrical conductors, enhancing electron transfer to facilitate the effective separation of photoelectrons from g-C_3N_4 and EY. (3) By functioning as photoelectron generators, the MOFs enhance the efficiency of H_2 production.

Photoelectrocatalytic investigations

To substantiate the solar hydrogen production findings, we carried out a photoelectrochemical analysis of the catalysts prepared in our study. The charge transfer properties and resistance of various composites were investigated through electrochemical impedance spectroscopy (EIS) analysis. The Nyquist plots of the EIS spectra, along with the equivalent circuit diagram, were acquired in a dark environment at a bias of 0.2 V. The frequency range covered during the measurements extended from 1 to 10^6 Hz, as depicted in Fig. 6(a). In the circuit diagram (inset of Fig. 6(a)), R_S denotes the series resistance, encompassing the resistance contributed by both ITO (indium tin oxide) and the counter electrode. R_{CT} represents the charge transfer resistance occurring at the photocatalyst interface. The presence of the large parabola in the high-frequency region suggests an increase in transportation and exchange resistance from the ITO to the counter electrode.[29] The R_{CT} value suggests a sluggish charge recombination process or a diminished charge recombination rate. The EIS curves suggest a sequential increase in the arc radius as follows: UiO-66-D@g-C_3N_4/Ni < UiO-66@g-C_3N_4/Ni < UiO-66-D < UiO-66. A smaller semi-circular diameter in the Nyquist plot generally indicates a reduced interfacial charge transfer resistance, leading to enhanced charge carrier transfers and improved photocatalytic activity.[15] This implies that UiO-66-D is a highly efficient electron-conducting catalyst compared to pristine UiO-66. Moreover, UiO-66-D combined with g-C_3N_4 plays an important role, not only in effectively reducing mechanical degradation, but also in significantly enhancing the diffusion of electrolyte ions. This synergistic effect is crucial in optimizing the overall performance of the system. This indicates that the UiO-66-D@g-C_3N_4/Ni composite exhibits a reduced interfacial charge transfer resistance compared to UiO-66@g-C_3N_4/Ni, leading to an enhanced photocatalytic activity. Additionally, the ternary UiO-66-D@g-C_3N_4/Ni composite benefits from the g-C_3N_4 moieties, which facilitate the fastest electron migration ability, effectively extending the charge transport behaviour between the electron–hole pairs in the system.

In contrast, the transient photocurrent and cathodic polarization curves exhibit analogous trends to the photochemical
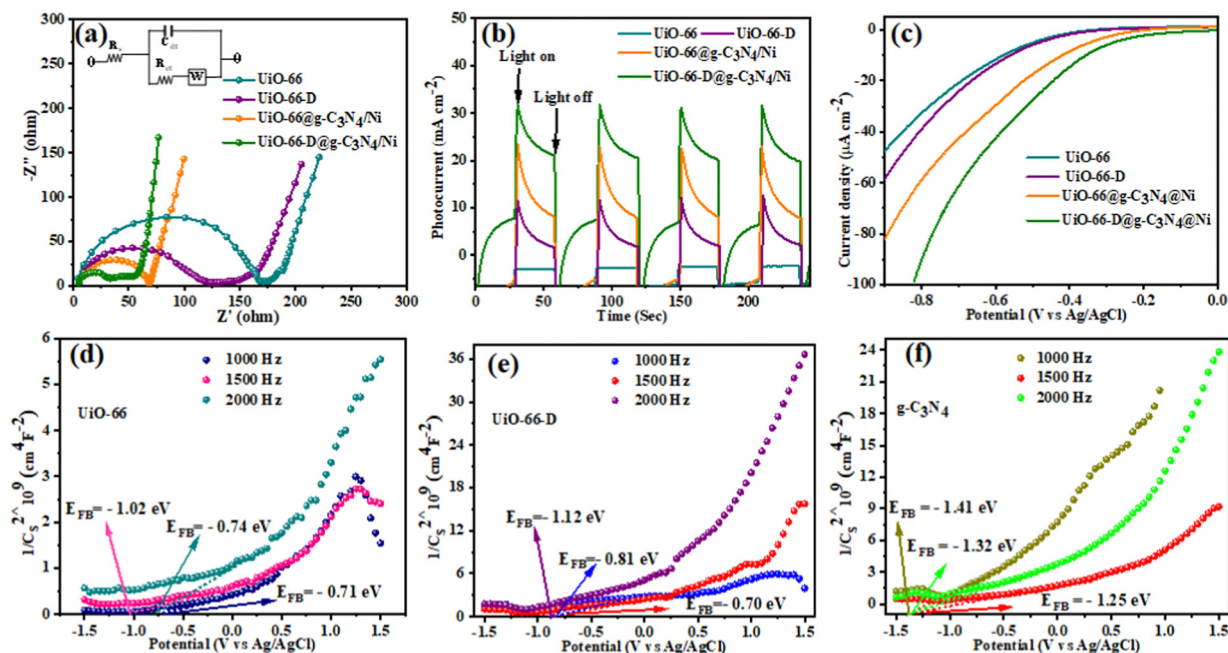
Fig. 6 (a) EIS Nyquist plots (inset: the equivalent circuit), (b) transient photocurrent, (c) linear sweep voltammetry curves, and (d)−(f) Mott−Schottky plots of UiO-66, UiO-66-D, and g-C_3N_4.

hydrogen production activity. UiO-66-D@g-C_3N_4/Ni demonstrates a superior transient photocurrent response of approximately 46.4 μA cm^{-2}, surpassing that of other photocatalysts (Fig. 6(b)). The ternary integrated hybrid composite demonstrated the highest photocurrent density, attributed to the effective charge migration path provided by g-C_3N_4, which significantly enhanced the interface connection and facilitated efficient electron transfer. The remarkable photocurrent response of the photocatalyst indicates the effective charge carrier generation and migration of charge carriers that ultimately enhance the photocatalytic performance.[46] To confirm this, we measured the LSV (linear sweep voltammetry) current of the electrodes, which confirms the anodic shift of the onset voltage for the MOF-based composite (Fig. 6(c)). Additionally, it is very well-acknowledged that the principle of reaction thermodynamics must be obeyed for photochemical H_2 generation with a sacrificial reagent:[47] $E_{CB} > E_{H_2/H^+} + E_R$, where E_{CB} represents the energy of the conduction band (or LUMO), E_{H_2/H^+} denotes the potential for H_2O reduction, and E_R corresponds to the overpotential for H_2O reduction. Though UiO-66 can provide electrons enabling proton reduction as explained above, the rate of hydrogen evolution is extremely low. The use of g-C_3N_4 can dramatically lower E_R while also increasing the rate of hydrogen generation. The activation overpotential of the hydrogen production process can represent the ability of g-C_3N_4 to reduce E_R. The onset overpotential of UiO-66-D@g-C_3N_4/Ni is lower than those of UiO-66@g-C_3N_4/Ni, UiO-66-D, and UiO-66. This finding indicates that the heterostructure formed by UiO-66-D and g-C_3N_4 can speed up the transfer of interfacial charges and increase the photocatalyst's hydrogen production capabilities.

To gain insight into band depletion and band alignment, we conducted measurements of the flat-band potential (E_{FB}) for both the UiO-66@g-C_3N_4/Ni and UiO-66-D@g-C_3N_4/Ni composites, and compared those with UiO-66-D and UiO-66 without illumination under the same electrolyte concentration using Mott–Schottky plots. As shown in Fig. 6(d) and (e), the positive slopes indicate that these materials exhibit n-type semiconductor behavior, with electrons as the dominant majority carrier. The estimated E_{FB} values of UiO-66, UiO-66-D, g-C_3N_4, UiO-66@g-C_3N_4/Ni, and UiO-66-D@g-C_3N_4/Ni were -0.74 V, −0.88 V, −1.41 V, −1.12 V, and −1.17 V vs. Ag/AgCl (i.e., −0.54 V, −0.68 V, −1.21 V, −0.92 V, and −0.97 V vs. NHE) from the x–intercept of the linear region of the M–S plots, respectively. Hence, for the conduction band minimum (CBM) of an n-type semiconductor, there exists a slight negative shift of approximately 0.1 V compared to the flat band potential.[48] The CBMs of UiO-66, UiO-66-D, g-C_3N_4, UiO-66@g-C_3N_4/Ni, and UiO-66-D@g-C_3N_4/Ni are about −0.64 V, −0.78 V, −1.31 V, −1.02 V, and −1.07 V (vs. NHE), which are well above the H^+/H_2 potential (Fig. S10, ESI†).

DFT calculations

In order to gain deeper insights into the enhanced charge carrier transfers observed in the UiO-66-D@g-C_3N_4 configuration, DFT calculations were conducted to investigate the interactions between UiO-66-D and g-C_3N_4. Typically, the work function ($\Phi = E_v − E_f$) is used to quantify the energy demand for the electron transfer of photogenerated electrons from the Fermi level (E_f) to the vacuum level (E_v). The evaluated electrostatic

potential for the UiO-66-D@g-C$_3$N$_4$ configuration is shown in Fig. 5(e), where the work functions of g-C$_3$N$_4$ and UiO-66-D were determined to be 5.94 and 5.06 eV, respectively. This signifies a photoinduced charge transfer from UiO-66-D to g-C$_3$N$_4$ at their heterojunction interface. As the result, an inherent electric field arises from the electron flow, promoting the effective separation of photogenerated carriers, resulting in a charge variation at the interface between g-C$_3$N$_4$ and UiO-66-D. Furthermore, to analyze the charge redistribution at the interface, we carried out computation, as shown in Fig. 5(f). Here, positive values signify an accumulation of electrons, whereas negative values suggest electron depletion. The findings highlight that the charge redistribution primarily results from the interaction between UiO-66-D and g-C$_3$N$_4$ at the interface. Clearly, the electron density around the UiO-66-D surface decreases, while it increases around g-C$_3$N$_4$ after the formation of the UiO-66-D@g-C$_3$N$_4$ heterostructure. This implies that the electron transfer occurs from the surface of UiO-66 to g-C$_3$N$_4$ within the UiO-66-D@g-C$_3$N$_4$ complex. Under the influence of the built-in electric field, photoelectrons are excited from UiO-66-D and accumulate at the g-C$_3$N$_4$ surface, facilitating the efficient separation of photogenerated holes and electrons. Consequently, photogenerated electrons are enriched around the g-C$_3$N$_4$ region.

In this report, it is envisioned that creating a heterojunction to establish interfacial bonds can reduce electron diffusion distances, enhance structural stability, expedite interfacial charge transfer, and stabilize the structure, ultimately resulting in improved intended properties and potentially unexpected ones as well. The favorable photophysical properties for g-C$_3$N$_4$ are the result of a two-dimensional framework formed by linking tri-s-triazine units through tertiary amines. To further accelerate the process, the deliberate construction of a heterojunction between g-C$_3$N$_4$ and suitably tuned Zr-MOF induces a spatial segregation of electrons and holes, positioning them on opposite sides of the junction, as shown in Fig. 1(a). This phenomenon serves to mitigate charge recombination, ultimately resulting in enhanced photocatalytic efficiency.

Conclusion

In conclusion, the integration of defects within the UiO-66@g-C$_3$N$_4$/Ni photocatalyst resulted in significantly enhanced hydrogen evolution performance. This research underscores the importance of defect-induced local strain and the modification of the electronic structure at the interface connecting UiO-66, g-C$_3$N$_4$, and Ni NPs, highlighting their contributions to superior catalytic activity. Tunable ligand-oriented defect engineering is employed to fine-tune the photonic and electrical properties of the UiO-66 framework. Experimental findings demonstrate that introducing unsaturation in UiO-66 and appropriately coordinating Ni in UiO-66-D@g-C$_3$N$_4$/Ni result in a substantial increase in the hydrogen production rate of 2.6 mmol g^{-1} h^{-1} with an AQY of 6.41% at 420 nm, compared to the Zr-MOFs benchmark photocatalyst. As anticipated, a

comprehensive set of photoelectrochemical and spectroscopic analyses provided valuable insights into the electron-transfer pathway, clearly demonstrating the accelerated kinetics and enhanced electron–hole pair dissociation in UiO-66-D@g-C$_3$N$_4$/Ni compared to UiO-66@g-C$_3$N$_4$/Ni and other systems. The positive outcomes seen from this study can be anticipated to apply to modulated MOFs, ZIFs, and core–shell MOFs/ZIFs, leading to notably improved solar energy conversion capabilities.

Conflicts of interest

There are no conflicts to declare.

Acknowledgements

References

1 (a) S. Navalon, A. Dhakshinamoorthy, M. Alvaro, B. Ferrer and H. García, Metal–Organic Frameworks as Photocatalysts for Solar-Driven Overall Water Splitting, Chem. Rev., 2023, **123**, 445–490; (b) S. Gonuguntla, R. Kamesh, U. Pal and D. Chatterjee, Dye sensitization of TiO$_2$ relevant to photocatalytic hydrogen generation: Current research trends and prospects, J. Photochem. Photobiol., C, 2023, **57**, 100621–100649.

2 (a) S. Gonuguntla, S. Sk, A. Tripathi, R. Thapa, G. Jonnalagadda, C. Nayak, D. Bhattacharyya, S. N. Jha, A. V. Sesha Sainath, V. Perupogu and U. Pal, Anisotropic phenanthroline-based ruthenium polymers grafted on a titanium metal-organic framework for efficient photocatalytic hydrogen evolution, Commun. Chem., 2022, **5**, 165–177; (b) P. Salcedo-Abraira, R. Serrano-Nieto, C. Biglione, M. Cabrero-Antonino, S. M. F. Vilela, A. A. Babaryk, D. Tilve-Martínez, A. Rodriguez-Dieguez, S. Navalon, H. Garcia and P. Horcajada, Two Cu-Based Phosphonate Metal–Organic Frameworks as Efficient Water-Splitting Photocatalysts, Chem. Mater., 2023, **35**, 4211–4219.

3 L. Fang, T. Huang, H. Lu, X.-L. Wu, Z. Chen, H. Yang, S. Wang, Z. Tang, Z. Li, B. Hu and X. Wang, Biochar-based materials in environmental pollutant elimination, H2 production and CO2 capture applications, Biochar, 2023, **5**, 42.

4 Y. Zhang, H. Liu, F. Gao, X. Tan, Y. Cai, B. Hu, Q. Huang, M. Fang and X. Wang, Application of MOFs and COFs for photocatalysis in CO$_2$ reduction, H$_2$ generation, and environmental treatment, EnergyChem, 2022, **4**, 100078–100121.

5 T. Hisatomi, J. Kubota and K. Domen, Recent advances in semiconductors for photocatalytic and photoelectrochemical water splitting, *Chem. Soc. Rev.*, 2014, **43**, 7520–7535.

6 A. Gautam, S. Sk and U. Pal, Recent advances in solution assisted synthesis of transition metal chalcogenides for photo-electrocatalytic hydrogen evolution, *Phys. Chem. Chem. Phys.*, 2022, **24**, 20638–20673.

7 M.-B. Majewski, A.-W. Peters, M.-R. Wasielewski, J.-T. Hupp and O.-K. Farha, Metal–Organic Frameworks as Platform Materials for Solar Fuels Catalysis, *ACS Energy Lett.*, 2018, **3**, 598–611.

8 Y. He, C. Li, X.-B. Chen, Z. Shi and S. Feng, Visible-Light-Responsive UiO-66(Zr) with Defects Efficiently Promoting Photocatalytic CO_2 Reduction, *ACS Appl. Mater. Interfaces*, 2022, **14**, 28977–28984.

9 K. L. Svane, J. K. Bristow, J. D. Galeb and A. Walsh, Vacancy defect configurations in the metal–organic framework UiO-66: energetics and electronic structure, *J. Mater. Chem. A*, 2018, **6**, 8507–8513.

10 Z. Qian, R. Zhang, H. Hu, Y. Xiao, H. Li, X. Sun and T. Ma, Decoration of Defective Sites in Metal–Organic Frameworks to Construct Tight Heterojunction Photocatalyst for Hydrogen Production, *Sol. RRL*, 2023, **7**, 2300547–2300556.

11 S. Sk, A. Jamma, D. S. Gavali, V. Bhasin, R. Ghosh, K. Sudarshan, R. Thapa and U. Pal, Modulated Ultrathin NiCo-LDH Nanosheet Decorated Zr^{3+}-Rich Defective NH_2-UiO-66-nanostructure for Efficient Photocatalytic Hydrogen Evolution, *ACS Appl. Mater. Interfaces*, 2023, **15**(48), 55822–55836.

12 C. Zhao, H. Jiang, Q. Liang, M. Zhou, Y. Zhang, Z. Li and S. Xu, NH_2-UiO-66 with heterogeneous pores assists zinc indium sulfide in accelerating the photocatalytic H_2 evolution under visible-light irradiation, *Sol. Energy*, 2020, **207**, 599–608.

13 X. Ma, L. Wang, Q. Zhang and H.-L. Jiang, Switching on Photocatalysis of Metal–Organic Frameworks by Engineering Structural Defects, *Angew. Chem., Int. Ed.*, 2019, **58**, 12175–12182.

14 A.-K. Singh, S. Gonuguntla, B. Mahajan and U. Pal, Noble metal-free integrated $UiO-66-PANI-Co_3O_4$ catalyst for visible-light-induced H_2 production, *Chem. Commun.*, 2019, **55**, 14494–14497.

15 S. K. Saddam, I. Mondal, A. Mahata, B.-M. Abraham, C. Nayak, D. Bhattacharyya, S.-N. Jha, R. Ghosh and U. Pal, Function of Defects in $NH_2-MIL-125@PANI@Co_3O_4$ Photocatalyst for Efficient Hydrogen Evolution, *ACS Appl. Energy Mater.*, 2022, **5**, 12324–12335.

16 W.-J. Ong, L.-L. Tan, Y.-H. Ng, S.-T. Yong and S.-P. Chai, Graphitic Carbon Nitride ($g-C_3N_4$) Based Photocatalysts for Artificial Photosynthesis and Environmental Remediation: Are We a Step Closer to Achieving Sustainability, *Chem. Rev.*, 2016, **116**, 7159–7329.

17 R. Wang, L. Gu, J. Zhou, X. Liu, F. Teng, C. Li, Y. Shen and Y. Yuan, Quasi-Polymeric Metal–Organic Framework UiO-66/$g-C_3N_4$ Heterojunctions for Enhanced Photocatalytic Hydrogen Evolution under Visible Light Irradiation, *Adv. Mater. Interfaces*, 2015, **2**, 1500037–1500042.

18 Z. Yang, X. Xu, X. Liang, C. Lei, Y. Cui, W. Wu, Y. Yang, Z. Zhang and Z. Lei, Construction of heterostructured MIL-125/Ag/$g-C_3N_4$ nanocomposite as an efficient bifunctional visible light photocatalyst for the organic oxidation and reduction reactions, *Appl. Catal., B*, 2017, **205**, 42–54.

19 D. A. Giannakoudakis, N. A. Travlou, J. Secor and T. J. Bandosz, Oxidized $g-C_3N_4$ Nanospheres as Catalytically Photoactive Linkers in MOF/$g-C_3N_4$ Composite of Hierarchical Pore Structure, *Small*, 2017, **13**, 1601758–1601767.

20 S. Panneri, M. Thomas, P. Ganguly, B. N. Nair, A. P. Mohamed and K. G. K. Warrier, Hareesh. U. S. C_3N_4 anchored ZIF 8 composites: photo-regenerable, high-capacity sorbents as adsorptive photocatalysts for the effective removal of tetracycline from water, *Catal. Sci. Technol.*, 2017, **7**, 2118–2128.

21 X. Wei, C. Shao, X. Li, N. Lu, K. Wang, Z. Zhang and Y. Liu, Facile in situ synthesis of plasmonic nanoparticles-decorated $g-C_3N_4$/TiO_2 heterojunction nanofibers and comparison study of their photo synergistic effects for efficient photocatalytic H_2 evolution, *Nanoscale*, 2016, **8**, 11034–11043.

22 T. Li, J.-D. Cui, M.-L. Xu, R. Li, L.-M. Gao, P.-L. Zhu, H. Q. Xie and K. Li, Engineering a hetero-MOF-derived TiO_2–Co_3O_4 heterojunction decorated with nickel nanoparticles for enhanced photocatalytic activity even in pure water, *CrystEngComm*, 2020, **22**, 5620–5627.

23 X.-L. Liu, R. Wang, M. Y. Zhang, Y. P. Yuan and C. Xue, Dye-sensitized MIL-101 metal organic frameworks loaded with Ni/NiO_x nanoparticles for efficient visible-light-driven hydrogen generation, *APL Mater.*, 2015, **3**, 104403–104409.

24 P. Basyach, J. Deb, S. Sk, U. Pal, M. Gogoi, G. N. Sastry and L. Saikia, Controlled Ni doping on a $g-C_3N_4$/$CuWO_4$ photocatalyst for improved hydrogen evolution, *Phys. Chem. Chem. Phys.*, 2023, **25**, 23033–23046.

25 P. Deng, M. Ga, X. Zhang, Z. Li and Y. Hou, Non-noble-metal Ni nanoparticles modified N-doped $g-C3N4$ for efficient photocatalytic hydrogen evolution, *Int. J. Hydrog. Energy*, 2019, **44**, 30084–30092.

26 L. T. Hoa, L. Thi, T. Nhi, L. Van, T. Són, N. L. M. Linh, H. V. M. Hai and D. Q. Khieu, Single-Atom Ni Heterogeneous Catalysts Supported UiO-66 Structure: Synthesis and Catalytic Activities, *J. Nanomater.*, 2021, 1–16.

27 X. Wang, N. Fu, J.-C. Liu, K. Yu, Z. Li, Z. Xu, X. Liang, P. Zhu, C. Ye, A. Zhou, A. Li, L. Zheng, L.-M. Liu, C. Chen, D. Wang, Q. Peng and Y. Li, Atomic Replacement of PtNi Nanoalloys within Zn-ZIF-8 for the Fabrication of a Multisite CO_2 Reduction Electrocatalyst, *J. Am. Chem. Soc.*, 2022, **144**, 23223–23229.

28 Z. Fang, B. Bueken, D. E. D. Vos and R. A. Fischer, Defect-Engineered Metal–Organic Frameworks, *Angew. Chem., Int. Ed.*, 2015, **54**, 7234–7254.

29 A. D. Vos, K. Hendrickx, P. V. D. Voort, V. V. Speybroeck and K. Lejaeghere, Missing Linkers: An Alternative Pathway to UiO-66 Electronic Structure Engineering, *Chem. Mater.*, 2017, **29**, 3006–3019.

30 M. A. Nasalevich, C. H. Hendon, J. G. Santaclara, K. Svane, B. V. Linden, S. L. Veber, M. V. Fedin, A. J. Houtepen,

M. A. V. Veen, F. Kapteijn, A. Walsh and J. Gascon, Electronic origins of photocatalytic activity in d^0 metal organic frameworks, *Sci. Rep.*, 2016, **6**, 23676–23685.

31 D. Gao, Y. Zhang, H. Yan, B. Li, Y. He, P. Song and R. Wang, Construction of UiO-66@MoS$_2$ flower-like hybrids through electrostatically induced self-assembly with enhanced photodegradation activity towards lomefloxacin, *Sep. Purif. Technol.*, 2021, **265**, 118486–118497.

32 A. Wang, Y. Zhou, Z. Wang, M. Chen, L. Sun and X. Liu, Titanium incorporated with UiO-66(Zr)-type Metal–Organic Framework (MOF) for photocatalytic application, *RSC Adv.*, 2016, **6**, 3671–3679.

33 Y.-P. Yuan, L.-W. Ruan, J. Barber, S. C. J. Loo and C. Xue, Hetero-Nanostructured Suspended Photocatalysts for Solar-to-Fuel Conversion, *Energy Environ. Sci.*, 2014, **7**, 3934–3952.

34 J. Chen, F. Chao, X. Ma, Q. Zhu, J. Jiang, J. Ren, Y. Guo and Y. Lou, Synthesis of flower-like CuS/UiO-66 composites with enhanced visible-light photocatalytic performance, *Inorg. Chem. Commun.*, 2019, **104**, 223–228.

35 P. Ganguly, M. Harb, Z. Cao, L. Cavallo, A. Breen, S. Dervin, D. D. Dionysiou and S. C. Pillai, 2D Nanomaterials for Photocatalytic Hydrogen Production, *ACS Energy Lett.*, 2019, **4**, 1687–1709.

36 S. Sk, C. S. Vennapoosa, A. Tiwari, B. M. Abraham, M. Ahmadipour and U. Pal, Polyaniline encapsulated Ti-MOF/CoS for efficient photocatalytic hydrogen evolution, *Int. J. Hydrog. Energy*, 2022, **47**, 33955–33965.

37 G. C. Shearer, S. Chavan, J. Ethiraj, J. G. Vitillo, S. Svelle, U. Olsbye, C. Lamberti, S. Bordiga and K. P. Lillerud, Tuned to Perfection: Ironing Out the Defects in Metal–Organic Framework UiO-66, *Chem. Mater.*, 2014, **26**, 4068–4071.

38 M. H. Hassan, A. B. Soliman, W. A. Elmehelmey, A. A. Abugable, S. G. Karakalos, M. Elbahri, A. Hassanien and M. H. Alkordi, A Ni-loaded, metal–organic framework–graphene composite as a precursor for in situ electrochemical deposition of a highly active and durable water oxidation nanocatalyst, *Chem. Commun.*, 2019, **55**, 31–34.

39 X. Ma, L. Wang, Q. Zhang and H.-L. Jiang, Switching on the Photocatalysis of Metal–Organic Frameworks by Engineering Structural Defects, *Angew. Chem., Int. Ed.*, 2019, **58**, 12175–12179.

40 A. Indra, P. W. Menezes, K. Kailasam, D. Hollmann, M. Schroder, A. Thomas, A. Bruckner and M. Driess, Nickel as a co-catalyst for photocatalytic hydrogen evolution on graphitic-carbon nitride (sg-CN): what is the nature of the active species?, *Chem. Commun.*, 2016, **52**, 104–107.

41 C. Cheng, L. Mao, X. Kang, C. L. Dong, Y. C. Huang, S. Shen, J. Shi and L. Guo, A high-cyano groups-content amorphous-crystalline carbon nitride isotype heterojunction photocatalyst for high-quantum-yield H2 production and enhanced CO2 reduction, *Appl. Catal., B*, 2023, **331**, 122733–122832.

42 J. Zou, G. Liao, J. Jiang, Z. Xiong, S. Bai, H. Wang, P. Wu, P. Zhang and X. Li, *In-situ* Construction of Sulfur-doped g-C$_3$N$_4$/defective g-C$_3$N$_4$ Isotype Step-scheme Heterojunction for Boosting Photocatalytic H$_2$ Evolution, *Chin. J. Struct. Chem.*, 2022, **41**, 2201025–2201033.

43 A. Tiwari, N. V. Krishna, L. Giribabu and U. Pal, Hierarchical Porous TiO$_2$ Embedded Unsymmetrical Zinc−Phthalocyanine Sensitizer for Visible-Light-Induced Photocatalytic H$_2$ Production, *J. Phys. Chem. C*, 2018, **122**, 495–502.

44 T. Lazarides, T. McCormick, P. Du, G. Luo, B. Lindley and R. Eisenberg, Making Hydrogen from Water Using a Homogeneous System Without Noble Metals, *J. Am. Chem. Soc.*, 2009, **131**, 9192–9194.

45 J. Xu, J. Gao, C. Wang, Y. Yang and L. Wang, NH$_2$-MIL-125(Ti)/graphitic carbon nitride heterostructure decorated with NiPdco-catalysts for efficient photocatalytic hydrogen production, *Appl. Catal., B*, 2017, **219**, 101–108.

46 P. Chowdhury, H. Gomaa and A. K. Ray, Sacrificial hydrogen generation from aqueous triethanolamine with Eosin Y-sensitized Pt/TiO$_2$ photocatalyst in UV, visible and solar light irradiation, *Chemosphere*, 2014, **121**, 54–56.

47 S. Sk, A. Tiwari, B. M. Abraham, N. Manwar, V. Perupogu and U. Pal, Constructing Cu/BN@PANI ternary heterostructure for efficient photocatalytic hydrogen generation: A combined experimental and DFT studies, *Int. J. Hydrog. Energy*, 2021, **46**, 27394–27408.

48 K. Sun, M. Liu, J. Pei, D. Li, C. Ding, K. Wu and H.-L. Jiang, Incorporating Transition-Metal Phosphides into Metal-Organic Frameworks for Enhanced Photocatalysis, *Angew. Chem., Int. Ed.*, 2020, **132**, 22749–22755.